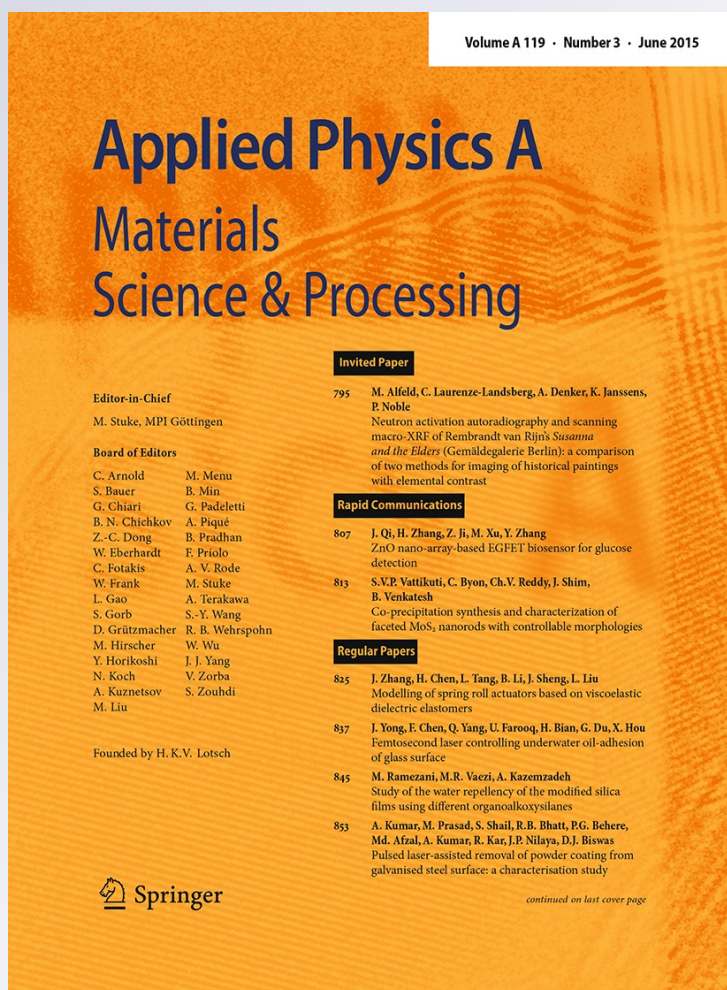# *Thermal characterization of ZnBeMnSe mixed compounds by means of photopyroelectric and lock-in thermography methods*

K. Strzałkowski, D. Dadarlat, M. Streza & J. Zakrzewski

Volume A 119 · Number 3 · June 2015

Applied Physics A

Materials Science & Processing

Springer

Springer

Thermal characterization of ZnBeMnSe mixed compounds by means of photopyroelectric and lock-in thermography methods

K. Strzałkowski · D. Dadarlat · M. Streza ·
J. Zakrzewski

Abstract In this work, a thermal characterization (measurement of dynamic thermal parameters) of quaternary $Zn_{1-x-y}Be_xMn_ySe$ mixed crystals was carried out. The crystals under investigation were grown from the melt by the modified high-pressure Bridgman method with different Be and Mn contents. The effect of Be and Mn contents on thermal properties of $Zn_{1-x-y}Be_xMn_ySe$ compounds was analyzed, by using the photopyroelectric (PPE) method in the back configuration (BPPE) for thermal diffusivity measurements and the PPE technique in the front configuration for thermal effusivity investigations. Infrared lock-in thermography was used in order to validate the BPPE results. The measured thermal effusivity and diffusivity allowed the calculation of thermal conductivity of the investigated materials.

1 Introduction

Diluted magnetic semiconductors (DMS) are materials with magnetic ions like Mn^{2+} implemented into the crystal structure [1]. DMS based on II–VI crystals such as $Zn_{1-x-y}Be_xMn_ySe$ mixed compounds with the manganese are very promising materials due to their unique magnetic and optical properties [2] with potential application in the design of the miniature magnetic field sensors, magnetic random access memory, spin transistors and applications of spin-based electronics in quantum informatics [3, 4]. $Zn_{1-x-y}Be_xMn_ySe$ semiconductors were proposed as a spin filter layers [5] with possible applications in memory technologies and also as base materials for magnetic resonant tunneling diodes (MRTD), achieving a voltage control over the spin relaxation [6, 7]. Manganese exhibits a relatively high solubility in many II–VI binary compounds, behaving like an isoelectronic atom, so n-type and p-type doping is possible. Optimized growth of lattice-matched GaAs and conduction band offset alignment was obtained by varying Be content in $Zn_{1-x-y}Be_xMn_ySe$ crystals. The beryllium content on II–VI ternary and quaternary compounds plays also a significant role for hardening and stability of the crystal lattice [8]. From an application's point of view, the thermal investigations of such a material are of paramount importance. The aim of this work is to investigate the thermal properties of $Zn_{1-x-y}Be_xMn_ySe$ mixed crystals as a function of Be and Mn contents. The thermal diffusivity can be obtained with various methods [9–12]. In this paper, the thermal diffusivity of the investigated materials is obtained with PPE technique [13–15] in the back detection configuration, coupled with the chopping frequency of the incident radiation scanning procedure. In order to validate the results obtained by PPE calorimetry, lock-in thermography technique is used for determining the thermal diffusivity of the crystals. The PPE method in the front detection configuration, together with the thickness scanning procedure (TWRC), is applied in order to obtain the crystals' thermal effusivity. The values obtained for the thermal diffusivity and effusivity allow the determination of thermal conductivity. The thermal conductivity dependence of the investigated materials on their composition is analyzed.

K. Strzałkowski (✉) · J. Zakrzewski
Institute of Physics, Faculty of Physics, Astronomy and
Informatics, Nicolaus Copernicus University, Grudziadzka 5,
87-100 Torun, Poland
e-mail: skaroll@fizyka.umk.pl

D. Dadarlat · M. Streza
National R&D Institute for Isotopic and Molecular
Technologies, Donath Str. 65-103, POB 700,
400293 Cluj-Napoca, Romania

Springer

2 Materials and methods

The crystals were grown from high-purity powders of ZnSe, Be, Mn and Se with the high-pressure modified Bridgman–Stockbarger method under argon overpressure of about 150 atm [8]. The crystal rods were cut perpendicular to the growth axis into about 1.5-mm-thick plates. Their thickness was measured with a micrometer device (accuracy 10 µm). The samples were first grounded by using grinding powder (Al_2O_3, 10 µm in diameter), next polished with diamond paste (1 µm). The real composition of the investigated crystals was measured with the scanning electron microscopy/energy-dispersive spectroscopy (SEM/EDS) analysis. Measurements were performed with scanning transmission microscope SEM-LEO 1430VP, made by LEO Electron Microscopy Ltd, Cambridge, England, and X-ray spectrometer (energy-dispersive mode) Quantax 200, made by Bruker AXS Microanalysis GmbH, Berlin, Germany, with EDX XFlash 4010 detector. The results showed that the investigated samples were spatially uniform in composition. The Be content was calculated, assuming that the sum of cation (Zn, Mn, Be) content (in at.%) is equal to that of Se anion. The structure of the measured crystalline alloys was determined with X-ray diffraction method, which confirmed that the samples exhibited a sphalerite structure. The starting composition, EDS results and the thickness of the investigated $Cd_{1-x-y}Zn_xMg_ySe$ samples are listed in Table 1.

The experimental setup for the BPPE measurements [16] consisted of a green, current-modulated DPSS (diode-pumped solid-state) laser (532 nm) with the output power of about 50 mW, a $LiTaO_3$ detector (0.54 mm thickness) with Cr+Au electrodes and a SR830 lock-in processing of the measured signal. The laser spot was set to about 2 mm in diameter to satisfy assumption about one-dimensional heat propagation through the sample. In this configuration, the sample is placed onto the sensor, and it is directly irradiated. A thin layer of ethylene glycol (effusivity 890 W s$^{1/2}$ m^{-2} K^{-1}, diffusivity 9.36 × 10^{-8} m^2 s^{-1}

Table 1 The composition and the thickness of the investigated $Zn_{1-x-y}Be_xMn_ySe$ crystal plates

Starting composition		Results of analysis		Thickness (mm)
x	y	x	y	
0.00	0.00	–	–	1.28
0.05	0.05	0.05	0.05	1.44
0.05	0.15	0.05	0.16	1.19
0.05	0.25	0.05	0.28	1.05
0.10	0.05	0.11	0.05	1.55
0.15	0.05	0.18	0.05	1.27
0.25	0.05	0.26	0.05	1.15

[16]) served as a coupling fluid between the sample and the sensor. To protect the detector from the scattered light, a black diaphragm was used. Frequency scans were performed in the 0.3–15 Hz range, with 0.3 Hz single step. A blackening procedure with a thin carbon layer (<10 µm) was applied to the samples in order to assure better optical absorption and optical opacity in the case of (semi) transparent samples.

The experimental setup in the front configuration (FPPE) (coupled with the thickness scanning procedure) consisted of a red He–Ne laser (Melles Griot, 30 mW) modulated with an acousto-optical modulator, a 215-µm-thick $LiTaO_3$ sensor coated with Cr+Au and a SR830 lock-in amplifier [16]. In this detection configuration, the laser directly illuminates the sensor. The measured samples were inserted into the detection cell as a backing material, so the blackening procedure was not needed. Ethylene glycol was used as coupling fluid between the sample and the sensor. During the scanning procedure, the coupling fluid was compressed starting from an initial value of about 0.5 mm. The scan was performed by a 9062M-XYZ-PPP Gothic-Arch-Bearing Picomotor with a single step of 6 µm. The control of the parallelism between the backing and the sensor was assured by two 3- and 6-axis micrometric stages.

The experimental IR setup included a heat source, a waveform generator, an infrared camera and a computer for data acquisition. The thermal images were collected from the blackened samples placed on a stage and excited with a green DPSS current-modulated laser (532 nm, 500 mW-less). The IR camera (FLIR 7200 Series) equipped with a 320 × 256 pixel array of InSb detectors with the spectral response in the range of wavelengths from 1.5 µm up to 5 µm recorded the changes in the surface temperature of the specimens. The noise equivalent temperature difference (NETD) of this camera is lower than 20 mK. The signals delivered by the infrared camera and the reference frequency f_0 were sent to the lock-in detection module incorporated into the camera, which outputs the continuous component image ($f = 0$) as well as the amplitude and phase images of the f-component to a PC. The optical axis of the camera was perpendicular to the investigated surface.

All measurements presented in this paper were computer-controlled and performed at room temperature.

3 Theory

In a BPPE four-layer system, a blackened sample s is placed on a pyroelectric sensor p and the whole system is surrounded by air (see Fig. 1). Due to the fact that the blackening carbon layer is very thin (<10 µm) and

thermally very conductive, one can neglect its influence on the signal. Assuming a perfect sample-sensor thermal contact and a one-dimensional model of the heat propagation through the sandwich-like multilayered system, the complex PPE signal is given by the following expression [17, 18]:

$$V = \frac{2V_0 e^{-\sigma_s L_s}}{b_{sp} + 1} \frac{1 - e^{-2\sigma_p L_p}}{1 + R_{sp}e^{-2\sigma_p L_p} - (R_{sp} + e^{-2\sigma_p L_p})e^{-2\sigma_s L_s}}$$

(1)

where V_0 is an instrumental factor, ij represents s and p layers of the detection cell, respectively, $R_{ij} = (b_{ij} - 1)/(b_{ij} + 1)$ is the reflection coefficient of the thermal wave at ij interface, $b_{ij} = e_i/e_j$, where e is thermal effusivity, $\sigma_i = (1 + i)a_i$ is the complex diffusion coefficient, where a_i is the reciprocal of the thermal diffusion length μ_i, $a_i = 1/\mu_i$, $\mu_i = (2\alpha_i/\omega)^{1/2}$, ω is the angular modulation frequency and L_i is the thickness of the layer i. In order to eliminate the instrumental factor V_0, a normalization procedure with empty sensor was applied [14]. After normalization, assuming thermally thick regime for both the detector and the sample ($\mu_i < L_i$), one can calculate the thermal diffusivity using the amplitude [Eq. (2)] and/or the phase [Eq. (3)], respectively [16]:

$$\ln|V_n| = \ln \frac{2}{b_{sp} + 1} - L_s \left(\frac{\omega}{2\alpha_s}\right)^{1/2}$$

(2)

$$\Theta = \Theta_0 - L_s \left(\frac{\omega}{2\alpha_s}\right)^{1/2}$$

(3)

In this paper, the thermal diffusivity was calculated from the slope of the phase curve $\Theta = \Theta(f^{1/2})$.

It is well known that the PPE calorimetry is a contact technique, and the coupling fluid, always necessary when investigating solids, leads to uncontrolled errors. This is why we propose, for thermal effusivity investigations, an alternative configuration that combines the front detection (FPPE) with the thermal-wave-resonator-cavity (TWRC) method (scanning of the coupling fluid's thickness). In this configuration, one can monitor the type and thickness of the coupling fluid (with known thermal properties) and

obtain with higher accuracy the thermal effusivity of a solid sample (backing material). The FPPE–TWRC configuration consists of four layers disposed in the following order: air/pyroelectric sensor/coupling fluid/sample (see Fig. 1). In a one-dimensional heat propagation model, the normalized complex PPE signal is given by [19]:

$$V_n = \frac{1 - R_{21}e^{-2\sigma_1 L_1}}{1 - \rho_{21}e^{-2\sigma_1 L_1}} \frac{(e^{-\sigma_1 L_1} - 1) - \rho_{21}(e^{-\sigma_1 L_1} - e^{-2\sigma_1 L_1})}{(e^{-\sigma_1 L_1} - 1) - R_{21}(e^{-\sigma_1 L_1} - e^{-2\sigma_1 L_1})}$$

(4)

where

$$R_{21} = \frac{1 - b_{21}}{1 + b_{21}}$$

$$\rho_{21} = \frac{(1 - b_{21}) + \rho_{32}(1 + b_{21})e^{-2\sigma_2 L_2}}{(1 + b_{21}) + \rho_{32}(1 - b_{21})e^{-2\sigma_2 L_2}}$$

$$\rho_{32} = \frac{1 - b_{32}}{1 + b_{32}}$$

In this configuration, one can get the thermal parameters of each layer of the detection cell (if the thermal parameters of the other layers are known). In this paper, we have been focused only on the thermal effusivity of the sample inserted as backing material in the detection cell.

It was shown [20, 21] that lock-in thermography allows the thermal diffusivity measurement of solid samples starting from the phase images. Assuming that the thickness of the blackening layer is negligible with respect to the sample thickness, the heat source is punctual and the sample under investigation is thermally thick; the thermal diffusivity can be obtained according to the following expression:

$$\mu = \frac{1}{a} = \sqrt{\frac{\alpha}{\pi f}}$$

(5)

where a is the slope of the phase–distance graph and f is the excitation frequency.

4 Results and discussion

Figure 2 presents the behavior of the phase as a function of the square root of the modulation frequency for all investigated samples measured with PPE technique in the back detection configuration. The samples under investigation were polished.

For low frequencies of modulation, the curves exhibit a nonlinear character due to the thermally thin regime of the sample or/and the sensor. Consequently, linear fits have been performed in slightly different frequency ranges, according to the requirements of the theory. For the fitting procedure, the least square method was applied. Thermal
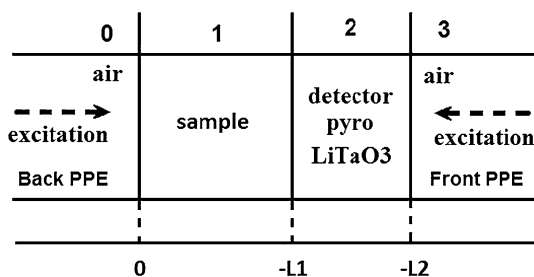

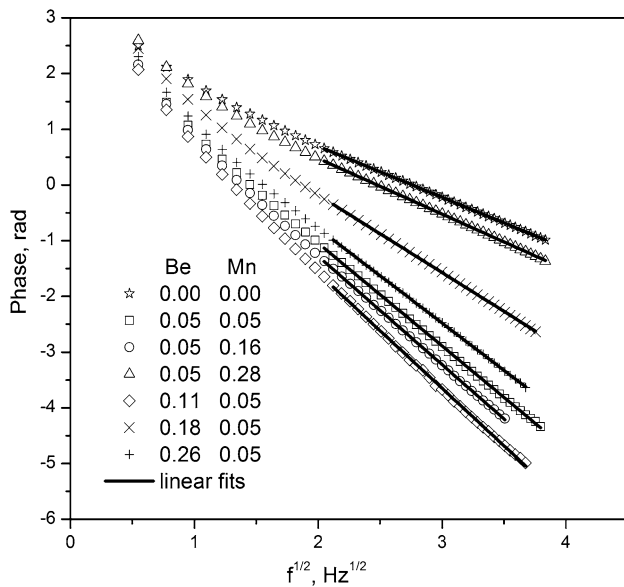**Fig. 1** Model of the cell in the back and front configuration for the PPE method

Fig. 2 PPE phases for the investigated samples as a function of the square root of the modulation frequency (the *dots* are experimental data, and the *lines* are linear fits)

Fig. 3 Thermal image of the phase of the $Zn_{0.9}Be_{0.05}Mn_{0.05}Se$ **a** sample measured at 2 Hz and corresponding phase profiles (**b**) taken from the thermal images, *points* correspond to measured data and *lines* are linear fits

diffusivities were calculated according to Eq. (3) from the slopes of the phase.

IRT phase images for $Zn_{0.9}Be_{0.05}Mn_{0.05}Se$ crystal with corresponding profiles are shown in Fig. 3a, b, respectively. The impact zone of the laser is represented by the constant phase zone in the center of the graph. The diameter of the laser can be estimated as about 300 μm (1 px = 30 μm), being considered a punctual excitation source. The field of view is 256 × 320 px (1 px = 30 microns), corresponding to 7.6 mm × 9.6 mm.

The thermal wave is propagating continuously, normal to the observed object surface, and also diffuses on the surface, symmetrically with respect to the excitation point source (represented here by the minimum of the phase profile, according to Fig. 3b), producing a phase delay compared to the laser impact zone. The thermal diffusivity of the specimen can be calculated from phase profiles, according to Eq. (5).

The values of the thermal diffusivity obtained with PPE method were smaller than those measured by lock-in thermography for all specimens; however, the differences were not large and lied within the error bars. The values obtained for the thermal diffusivity of $Zn_{0.9}Be_{0.05}Mn_{0.05}Se$ crystal, by PPE and IRT, are as follows: $(2.831 \pm 0.015) \times 10^{-6}$ m^2 s^{-1} and $(2.884 \pm 0.062) \times 10^{-6}$ m^2 s^{-1}. Salazar et al [22] have shown that these differences are mainly due to the presence of the coupling liquid between the sample and the sensor. The influence of the coupling fluid on the obtained thermal properties depends on the configuration of the system, on the value of the modulation frequency and on the
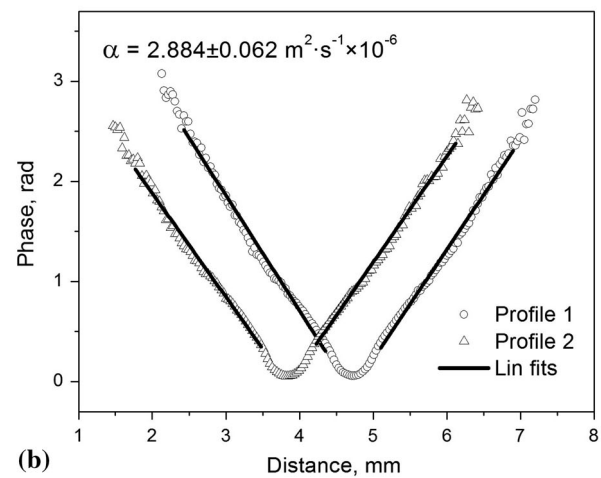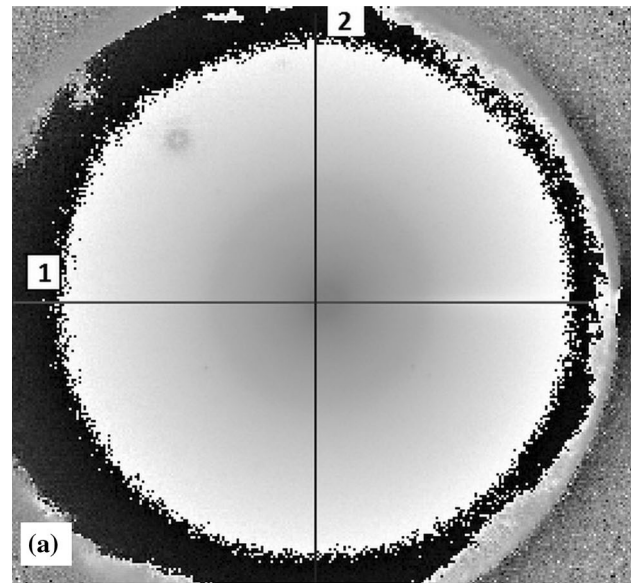
thermal and mechanical properties of the sample and the sensor. This is why we decided to use a non-contact method, the lock-in thermography, in order to validate the thermal diffusivity values obtained by BPPE.

Figure 4a, b reveal the phase behavior of $Zn_{0.9}Be_{0.05}Mn_{0.05}Se$ sample measured at 3 and 5 Hz using the thickness scanning procedure of the coupling fluid in FPPE configuration and the contour map of the precision of the fitting, respectively. At the applied frequencies, the sensor is thermally thin and the sample is thermally thick, while the coupling fluid passes from thermally thick to thermally thin regime during the thickness scan; consequently, the theoretical conditions imposed by the particular detection case are fulfilled.
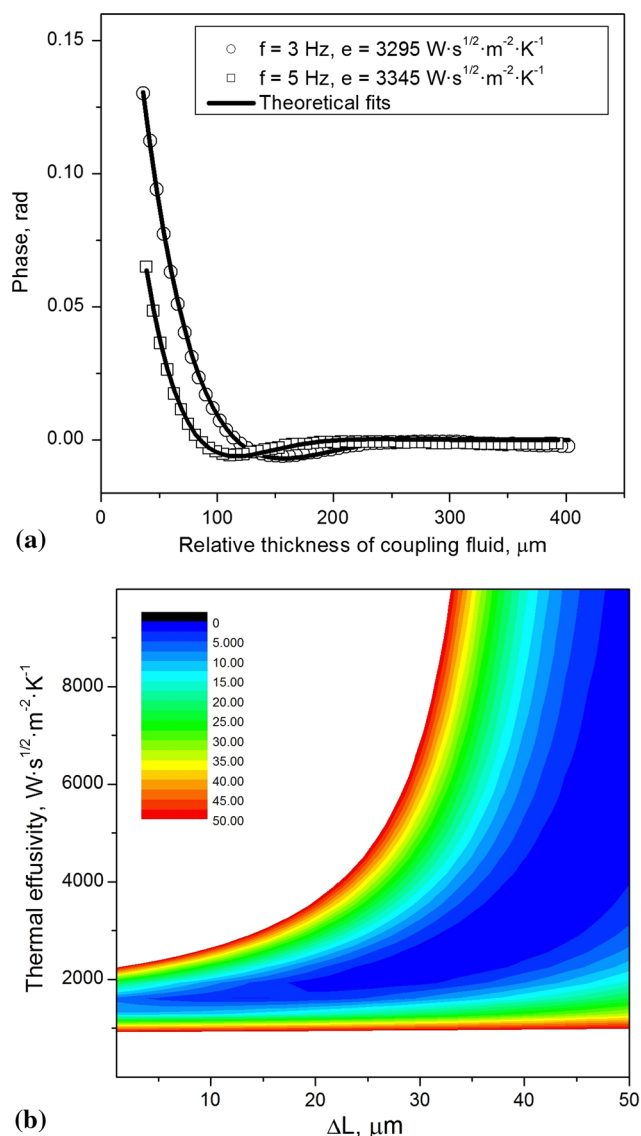
(a)

(b)

Fig. 4 Phase characteristics of the $Zn_{0.9}Be_{0.05}Mn_{0.05}Se$ sample (**a**) measured at 3 (*circles*) and 5 Hz (*squares*) with FPPE method. Experimental results are represented by *dots* and theoretical fittings [see. Eq. (4)] by lines. **b** represents the contour map of the fitting precision

The constant behavior of the phase in picture (a) is associated with the thermally thick regime of the coupling fluid, and this value is used for the normalization procedure. In order to obtain the thermal effusivity, a numerical analysis of Eq. (4) has been performed using the least square method with two fitting parameters: the thermal effusivity of the backing material (sample) and the absolute thickness of the coupling fluid (distance between the sample and the sensor). The best theoretical fits performed with the least square method and the obtained values of thermal effusivity can be seen in Fig. 4a.

The contour map as shown in Fig. 4b is connected with the precision of the fitting performed with Eq. (4). In the contour map, the x-axis represents the error in the absolute value of the thickness of the coupling fluid and the y-axis represents the thermal effusivity. A theoretical analysis indicates that the accuracy of the fitting depends on backing/liquid (e_3/e_2) effusivity ratio [16]. High effusivity ratios (5 or more) are associated with rather accurate location of the backing position, while thermal effusivity is obtained with low precision and reciprocal. For the investigated $Zn_{0.9}Be_{0.05}Mn_{0.05}Se$ sample, the ratio is about 3.7 and, as proved by the shape of the precision curves in Fig. 4b, the accuracy for the value of the thermal effusivity is rather good.

The contour map indicates the precision of the fit performed with Eq. (4) on the experimental data. X-axis represents the correction term in the measurement of the absolute coupling fluid's thickness. The shape of the contour curves can indicate a good localization of the position of the backing (when the contour curves are vertical), or a good precision in the value of thermal effusivity (when the contour curves are horizontal). In our measurements, the contour curves are horizontal, due to the rather close values of the thermal effusivity of the coupling fluid and backing material, and consequently, the precision in the value of thermal effusivity is good.

The thermal parameters of all measured samples are given in Table 2. Since for the given experimental condi-

Table 2 Thermal parameters of the investigated $Zn_{1-x-y}Be_xMn_ySe$ crystals

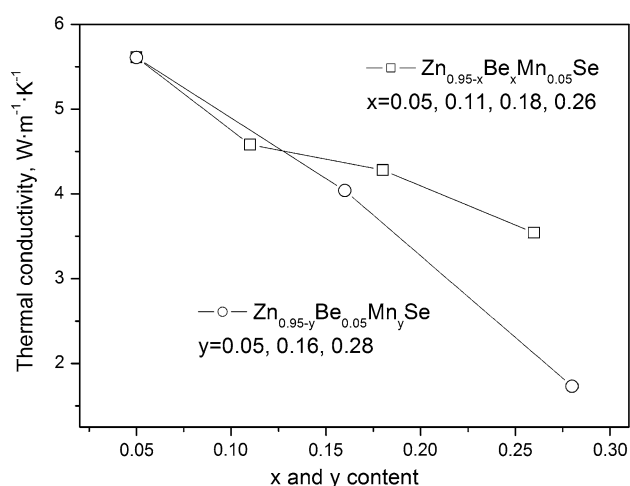| x	y	Thermal diffusivity $(m^2 s^{-1}) \times 10^{-6}$	Thermal effusivity $(W s^{1/2} m^{-2} K^{-1})$	Thermal conductivity $(W m^{-1} K^{-1})$
0.00	0.00	9.846 ± 0.030	5633 ± 35	17.676 ± 0.090
0.05	0.05	2.831 ± 0.015	3322 ± 25	5.612 ± 0.068
0.05	0.16	2.252 ± 0.012	2692 ± 24	4.044 ± 0.046
0.05	0.28	1.426 ± 0.016	1454 ± 17	1.731 ± 0.022
0.11	0.05	2.583 ± 0.014	2853 ± 27	4.585 ± 0.054
0.18	0.05	2.414 ± 0.015	2760 ± 25	4.283 ± 0.051
0.26	0.05	2.151 ± 0.014	2415 ± 25	3.546 ± 0.042

Fig. 5 Thermal conductivity dependence of $Zn_{1-x-y}Be_xMn_ySe$ crystals on the composition, lines were added for better visualization of the two sets of experiments, where x and y are varied independently; *squares* and *circles* represent crystals with varying Be and Mn contents, respectively

tions, the influence of the coupling fluid is negligible; the thermal diffusivity obtained by PPE technique was used for the calculation of thermal conductivity. Each sample was measured three times, and the resulted data were averaged. The uncertainty of the results is given as standard deviation.

The thermal effusivities as listed in Table 2 represent the average value computed at two excitation frequencies (3 and 5 Hz, respectively). The obtained values lie within 1 % deviation of the mean value. Thermal conductivity was calculated using relations between all parameters from the expression: $k = e\alpha^{1/2}$. The uncertainty of thermal conductivity was calculated using partial differentiation method as simply average errors, taking into account the uncertainty of thermal diffusivity and effusivity.

Binary (x and y equal 0) ZnSe sample was used as a test material. The obtained thermal conductivity (17.68 W m^{-1} K^{-1}) of this crystal remains in good agreement (19 W m^{-1} K^{-1}) with the literature data [23].

Figure 5 represents the thermal conductivities of all $Zn_{1-x-y}Be_xMn_ySe$ mixed crystals as a function of composition. The results were divided into two groups of crystals, depending on the composition.

In some sense, the quaternary $Zn_{1-x-y}Be_xMn_ySe$ compound is the mixture of ZnSe, BeSe and MnSe binary crystals, and consequently, its thermal properties are resultant of all components. One can see that the thermal conductivity decreases with increasing of beryllium (x) and manganese (y) contents. The thermal conductivity values of mixed compounds compared with binary ZnSe crystal decrease by a factor three to five. Similar phenomenon was

observed previously for ternary $Cd_{1-x}Mg_xSe$ [24] and quaternary $Cd_{1-x-y}Zn_xMg_ySe$ crystalline alloys with increasing magnesium content [25]. One can conclude that the addition of beryllium and manganese to the $Zn_{1-x-y}Be_xMn_ySe$ alloy enhances the concentration of the defects in the crystal. This effect [24, 25] is mainly due to the difference in atomic radius of the components, and, as a consequence, the periodic potential of lattice is perturbed. Every crystal imperfection in such a material becomes a potential scattering center for phonons, and consequently, the ability of the material to conduct the heat is reduced.

5 Conclusions

In this paper, a complete thermal characterization (measurement of dynamic—diffusivity, effusivity and conductivity—thermal parameters) of $Zn_{1-x-y}Be_xMn_ySe$ crystals grown by high-pressure modified Bridgman–Stockbarger method was carried out. The thermal diffusivity of the samples was obtained by PPE method in the back detection configuration. Lock-in thermography technique was used in order to validate the results obtained by PPE calorimetry.

The thermal effusivity values were derived from the PPE measurements in the front configuration coupled with the TWRC method. The measured thermal diffusivity and effusivity allowed the calculation of the thermal conductivity. The results presented for the reference binary ZnSe crystal are in good agreement with the reported data, supporting the suitability of the applied methods and the accuracy of the obtained results.

The thermal conductivity values of mixed $Zn_{1-x-y}Be_xMn_ySe$ crystals decreased by a factor from three to five compared with binary ZnSe sample. Indeed, we have shown that the addition of both beryllium and manganese enhances the occurrence of defects within the crystal lattice and accordingly, the thermal conductivity of the specimens. In conclusion, the presence of the defects and impurities in the crystal can strongly influence the semiconductors' thermal properties.

References

1. J.A. Gaj, J. Kossut, *Introduction to the Physics of Diluted Magnetic Semiconductors* (Springer, Springer Series in Materials Science, 2011)
2. D.M. Zayachuk, T. Slobodskyy, G.V. Astakhov, A. Slobodskyy, C. Gould, G. Schmidt, W. Ossau, L.W. Molenkamp, Phys. Rev. B **83**, 085308 (2011)
3. R. Fitzgerald, Phys. Today **53**, 23 (2000)
4. S.J. Pearton, C.R. Abernathy, D.P. Norton, A.F. Hebard, Y.D. Park, L.A. Boatner, J.D. Budai, Mat. Sci. Eng. R **40**, 137 (2003)
5. Yong Guo, Fei-Ruo Shen, Xin-Yi Chen, Appl. Phys. Lett. **101**, 012410 (2012)
6. Christian Ertler, Jaroslav Fabian, Phys. Rev. B **75**, 195323 (2007)
7. A. Frey, M. Ruth, R.G. Dengel, C. Schumacher, C. Gould, G. Schmidt, K. Brunner, L.W. Molenkamp, J. Crys. Growth **312**, 1036 (2010)
8. F. Firszt, S. Łęgowski, H. Męczyńska, J. Szatkowski, W. Paszkowicz, K. Godwod, J. Cryst. Growth **184/185**, 35 (1998)
9. D. Trefon-Radziejewska, J. Bodzenta, T. Łukasiewicz, Int. J. Thermophys. **34**, 813 (2013)
10. M. Pawlak, M. Malinski, Thermochim. Acta **599**, 23 (2015)
11. M. Pawlak, M. Maliński, F. Firszt, J. Pelzl, A. Ludwig, A. Marasek, Meas. Sci. Technol. **25**, 035204 (2014)
12. D. Korte-Kobylinska, E. Paclica, G. Bratina, M. Franko, Int. J. Thermophys. **35**, 1990 (2013)
13. D. Dadarlat, J. Therm. Anal. Calorim. **110**, 27 (2012)
14. M. Marinelli, F. Mercuri, U. Zammit, R. Pizzoferrato, F. Scudieri, D. Dadarlat, Phys. Rev. B **49**, 9523 (1994)
15. D. Dadarlat, D. Bicanic, H. Visser, F. Mercuri, A. Frandas, J. Am. Oil Chem. Soc. **74**, 273 (1995)
16. D. Dadarlat, Laser Phys. **19**, 1330 (2009)
17. M. Chirtoc, G. Mihailescu, Phys. Rev. B **40**, 9606 (1989)
18. A. Mandelis, M.M. Zver, J. Appl. Phys. **57**, 4421 (1985)
19. J. Shen, A. Mandelis, Rev. Sci. Instrum. **66**, 4999 (1995)
20. H.W. Carslaw, J.C. Jaeger, *Conduction of Heat in Solids*, 2nd edn. (Oxford University Press, London, 1959)
21. C. Boue, S. Hole, Infrared Phys. Technol. **55**, 376 (2012)
22. A. Salazar, A. Oleaga, Rev. Sci. Instrum. **83**, 014903 (2012)
23. O. Madelung, *Semiconductors: Data Handbook* (Springer, Berlin, Heidelberg, 2003)
24. M. Pawlak, F. Firszt, S. Łęgowski, H. Męczyńska, J. Gibkes, J. Pelzl, Int. J. Thermophys. **31**, 187 (2010)
25. K. Strzałkowski, Mater. Sci. Eng. B **184**, 80 (2014)